nature communications

Article

https://doi.org/10.1038/s41467-024-55280-0

Realizing high power factor and thermoelectric performance in band engineered $AgSbTe_2$

Received: 19 July 2024

Accepted: 6 December 2024

Published online: 02 January 2025

Check for updates

Yu Zhang [1,2,18], Congcong Xing [1,2,18], Dongyang Wang [3], Aziz Genç [4], Seng Huat Lee [5,6], Cheng Chang [7], Zhi Li [8], Luyao Zheng [2], Khak Ho Lim [9], Hangtian Zhu [2,10], Rabeya Bosry Smriti [2,11], Yu Liu [12], Shaobo Cheng [3], Min Hong [13], Xiaolei Fan [1,14], Zhiqiang Mao [6], Li-Dong Zhao [7], Andreu Cabot [15,16], Tiejun Zhu [1,17] & Bed Poudel [2]

$AgSbTe_2$ is a promising p-type thermoelectric material operating in the mid-temperature regime. To further enhance its thermoelectric performance, previous research has mainly focused on reducing lattice thermal conductivity by forming ordered nanoscale domains for instance. However, the relatively low power factor is the main limitation affecting the power density of $AgSbTe_2$-based thermoelectric devices. In this work, we demonstrate that hole-doped $AgSbTe_2$ with Sn induces the formation of a new impurity band just above the valence band maximum. This approach significantly improves the electrical transport properties, contrary to previous strategies that focused on reducing lattice thermal conductivity. As a result, we achieve a record-high power factor of 27 $\mu Wcm^{-1}K^{-2}$ and a peak thermoelectric figure of merit zT of 2.5 at 673 K. This exceptional performance is attributed to an increased hole concentration resulting from the formation of the impurity band and a lower formation energy of the defect complexes ($V_{Ag}^{1-} + Sn_{Sb}^{1-}$). Besides, the doped materials exhibit a significantly improved Seebeck coefficient by inhibiting bipolar conductivity and preventing the formation of n-type Ag_2Te. Additionally, the optimized $AgSbTe_2$ is used to fabricate a unicouple thermoelectric device that achieves energy conversion efficiencies of up to 12.1% and a high power density of 1.13 Wcm^{-2}. This study provides critical insights and guidance for optimizing the performance of p-type $AgSbTe_2$ in thermoelectric applications.

Thermoelectric (TE) devices provide a simple solution not only for power generation from waste heat but also for precise temperature control and localized cooling[1–4]. TE-based products have been widely utilized in consumer electronics, communications, medical, and automotive fields. The performance of a TE material is usually characterized by a dimensionless figure of merit, $zT = (S^2\sigma/\kappa)T$, where T is the absolute temperature, S is the Seebeck coefficient, σ is the electrical conductivity, and κ is the thermal conductivity[5].

The optimization of the performance of TE materials can be approached through two primary strategies; the reduction of the lattice thermal conductivity (κ_L) and the enhancement of the TE power factor (*PF*). These properties are interconnected, as any modification aimed at optimizing one of these parameters will inevitably influence the other.

$AgSbTe_2$ is a promising p-type TE material, particularly suitable for applications in the medium temperature range (473–673 K)[6–11]. This

A full list of affiliations appears at the end of the paper. e-mail: yzhangpeter@163.com; zhutj@zju.edu.cn; bup346@psu.edu

material exhibits inherently low thermal conductivity, attributable to its spontaneously formed micro/nanostructures and pronounced bond anharmonicity. Additionally, $AgSbTe_2$ demonstrates a high Seebeck coefficient, which is a consequence of its flat valence band with substantial degeneracy.

Compositional engineering has been widely used as an effective strategy to modulate the $AgSbTe_2$ band structure and carrier concentration, thereby enhancing TE performance[12–19]. For instance, heavy doping of $AgSbTe_2$ with Se/S effectively increases the hole concentration, leading to a significant improvement in the *PF* by facilitating the participation of multiple bands in charge transport[19]. Numerous studies have reported that the formation of nanoscale superstructures, triggered by enhanced cation ordering through doping with elements such as Cd[20], Hg[21], Yb[22], or Ag vacancies[23], results in remarkable increases in *zT* up to 2.6. This enhancement is primarily due to the notable reduction in κ_L to as low as $0.2\,W\,m^{-1}\,K^{-1}$[20]. However, despite such advances, the *PF* achieved in these studies remains below $20\,\mu Wcm^{-1}K^{-2}$, which is significantly lower than that of commercial Bi_2Te_3 materials. While a high *zT* value is crucial for achieving high TE device conversion efficiency, the relatively low *PF* continues to limit the overall output power of $AgSbTe_2$-based TE devices. Thus, further optimization is necessary to simultaneously enhance both *zT* and *PF* for practical applications.

Herein, we present a strategy to enhance the electrical transport properties of p-type $AgSbTe_2$ through the incorporation of Sn as an effective dopant. Sn doping is shown to significantly stabilize the $AgSbTe_2$ matrix by inhibiting the formation of n-type Ag_2Te and introducing an in-gap band slightly above the valence band maximum (VBM). We demonstrate that this compositional engineering strategy result in exceptionally high *PF* and *zT* values. Besides, using this optimized material, a unicouple TE device is fabricated and tested to validate the real application potential of this material.

Results and discussion

Polycrystalline $AgSbTe_2$ was synthesized via a multi-step process involving the initial melting of a stoichiometric mixture comprising elemental Ag, Sb, and Te. The resulting ingots were subsequently ground and re-consolidated utilizing spark plasma sintering, as detailed in the supplementary information (SI). At ambient temperature, $AgSbTe_2$ commonly exhibits a rock salt crystal structure, characterized by the random distribution of Ag and Sb ions within the cation sublattice, while Te occupies the anion sites. However, the phase diagram of Sb_2Te_3-Ag_2Te indicates that stoichiometric $AgSbTe_2$ undergoes thermodynamic instability at temperatures below 633 K, leading to its decomposition into Ag_2Te and Sb_2Te_3 phases[24,25]. Detailed investigations into the phase diagram have established that the single stable ternary phase encompasses a broad compositional range ($Ag_{1-x}SbTe_2$, $x = 0.06–0.28$). Consequently, the precise structural configuration of $AgSbTe_2$ and its stability remain ambiguous. To investigate the crystalline characteristics of the synthesized material, X-ray diffraction (XRD) analysis was conducted. The obtained XRD patterns revealed a predominant face-centered cubic (fcc) crystal structure consistent with $AgSbTe_2$. Furthermore, the presence of minor weak diffraction peaks was identified, corresponding to the monoclinic phase of Ag_2Te, which confirms the existence of both phases within the synthesized material (Fig. S1). This observation aligns with previous studies, which have consistently reported the presence of precipitated Ag_2Te phase and other impurities coexisting within the $AgSbTe_2$ matrix, regardless of the synthesis methodologies employed[13,15,17,19,20,23].

Given the semiconductor nature of Ag_2Te, characterized by a n-type conductivity, and its structural phase transition occurring around 425 K, even minimal concentrations of Ag_2Te can adversely impact the electrical transport properties of p-type $AgSbTe_2$. Therefore, suppressing the formation of Ag_2Te impurities becomes critical for optimizing the TE performance of $AgSbTe_2$.

The inherent instability of pristine $AgSbTe_2$ is primarily attributed to the presence of antibonding states near the Fermi level, as proved by crystal orbital Hamiltonian population analysis[26]. The antibonding states arise from the strong hybridization between Sb-5s and Te-5p orbitals, leading to the Te-5p antibonding states shift towards the valence band frontier. From an electronic structure perspective, such antibonding contributions constitute the primary states at the top of the valence band, thereby stimulating intrinsic instability through the formation of charge-compensated defect complexes. Consequently, $AgSbTe_2$ undergoes spontaneous phase decomposition, forming Ag_2Te and Sb_2Te_3 phases for instance. To suppress this instability, p-type doping emerges as an effective strategy to reduce the electron density associated with these antibonding states, thereby potentially enhancing the stability of the $AgSbTe_2$ matrix. To this end, our study aims at stabilizing the $AgSbTe_2$ matrix by incorporating trace amounts of Sn into the cationic sublattice (Fig. 1a). The preference for Sn^{2+} to substitute Sb^{3+} is based on its possession of one fewer valence electron, which facilitates the generation of additional holes, thereby contributing to the stabilization of the $AgSbTe_2$ structure.

XRD analysis confirmed that the Sn-doped material exhibited the cubic $AgSbTe_2$ phase, with no detectable presence of Ag_2Te (Fig. 1b). Ag_2Te absence was corroborated by differential scanning calorimetry (DSC) analysis, which indicated the suppression of the endothermic peak at 423 K associated with the β-Ag_2Te to α-Ag_2Te phase transition (Fig. 1c). High-resolution X-ray photoelectron spectroscopy (XPS) analysis, as depicted in Fig. 1d, shows only one Sn $3d$ doublet at 486.1 eV ($3d_{5/2}$). This is associated with a bivalent Sn state[27,28], further confirming the successful integration of Sn^{2+} into the $AgSbTe_2$ system. Overall, we observed the incorporation of Sn to effectively enhance the thermodynamic stability of $AgSbTe_2$ by suppressing the formation of Ag_2Te secondary phases.

To comprehensively understand the impact of Sn incorporation on the $AgSbTe_2$ structure, the electronic band structure (Fig. 2a, b) was analyzed and the formation energies of multiple defects (Fig. 2c, d) were determined using density functional theory (DFT) calculations. The computational analysis of the electronic band structure of pristine $AgSbTe_2$, as depicted in Fig. 2a, uncovers a semimetallic character with a pseudogap arising from the interplay between dispersive conduction bands and nearly flat valence bands, that aligns with previous research findings[6,9,21]. It is worth noting that previous optical reflectance assessments revealed a distinct band gap ranging from 0.30 to 0.35 eV[14,19,29], suggesting a semiconducting behavior. Conversely, DFT calculations and electrical conductivity analyzes portray either a semimetallic or metallic character[6,9,11,20]. This discrepancy may arise from the structural disorder of Ag and Sb atoms. DFT calculations typically assume ordered occupancy to establish the supercell, which can result in deviations from the actual disordered structure. Near the Fermi level, we observe the presence of light electron pockets and heavy hole pockets (predominantly formed by Te-5p orbitals), which suggests that the electrical conductivity in $AgSbTe_2$ primarily stems from high mobility electrons and low mobility holes. Furthermore, the flat VBM and degenerate valence band structure indicate a larger positive Seebeck coefficient for pristine $AgSbTe_2$ compared to other TE chalcogenides like PbTe[30,31] and SnTe[32,33].

Upon doping with Sn, notable changes occur in the band structure of $AgSbTe_2$. The VBM undergoes flattening at the Γ point, accompanied by significant band splitting, pointing at an enhancement of the Seebeck coefficient. Specifically, a new impurity band, highlighted in red color, emerges above the VBM due to the substitution of Sn^{2+} for Sb^{3+} (Fig. 2b). This impurity band is partially occupied, with the Fermi energy falling within its energy range. Consequently, thermal carrier generation triggers from the edge of the impurity band rather than the valence band edge. This mechanism results in additional holes in the valence band, as experimentally obtained from Hall measurements (Table S1). Similarly, dopants that introduce in-gap impurity levels,

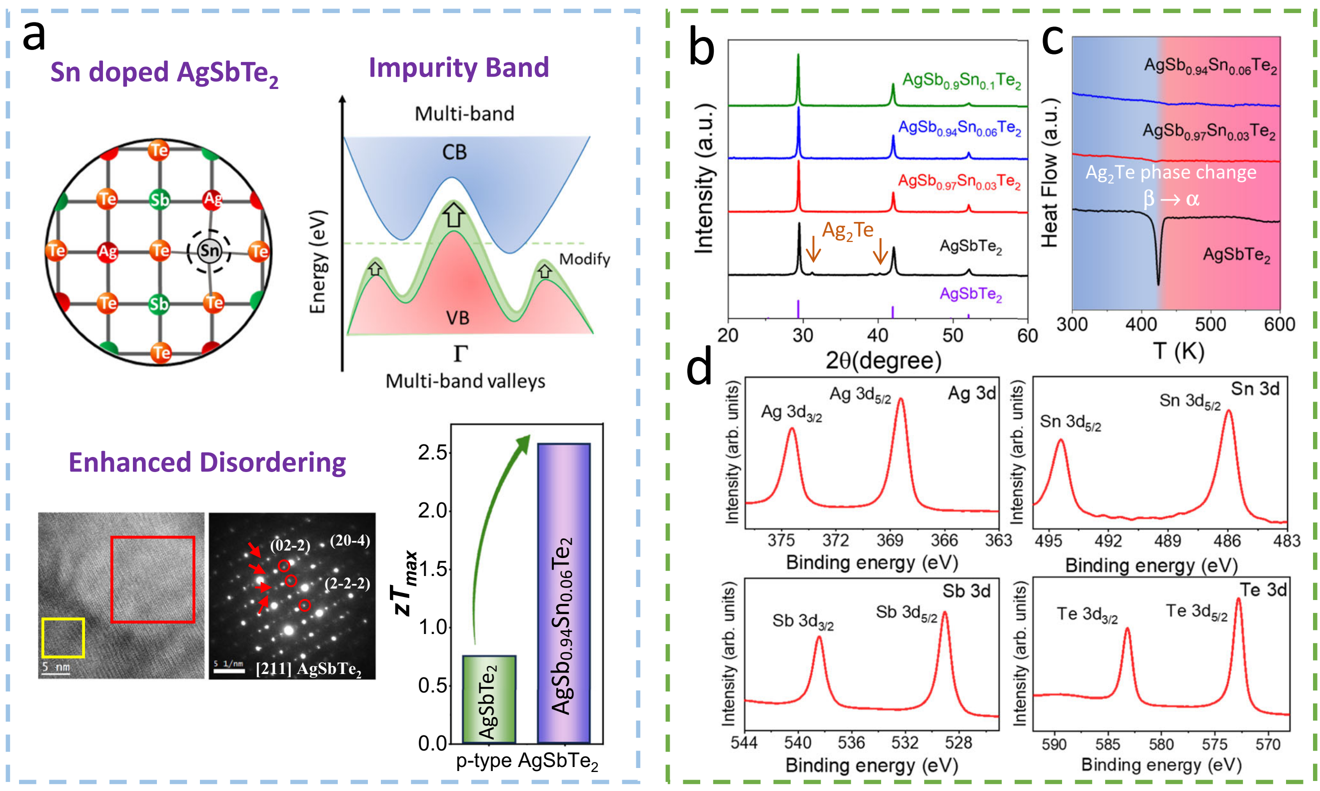

Fig. 1 | TE performance and characterizations on Sn doped $AgSbTe_2$ samples. a Schematic illustration of improved TE performance in Sn doped $AgSbTe_2$. **b** XRD patterns of as-synthesized $AgSb_{1-x}Sn_xTe_2$ pellets. **c** DSC curves of $AgSbTe_2$ and Sn-doped $AgSbTe_2$. **d** High-resolution XPS spectra of $AgSb_{0.94}Sn_{0.06}Te_2$ pellet.

thereby enhancing carrier density and electrical transport properties, have been identified in p-type $Cr_2Ge_2Te_6$[34] and $Cu_{1-x}Ag_xGaTe_2$[35,36] compounds for instance.

The negative formation energy of Ag vacancies (V_{Ag}^{1-}) suggests their spontaneous generation in undoped $AgSbTe_2$ (Fig. 2c). V_{Ag}^{1-} acts as an acceptor providing holes. However, the number of carriers is limited due to the self-compensating effect (compensate charge distortion by creating donor defects, such as Sb at Ag site, Sb_{Ag}^{1+}) that maintains charge neutrality in the system, resulting in a low net hole concentration in $AgSbTe_2$. In the case of $AgSb_{1-x}Sn_xTe_2$ (Fig. 2d), Sn doping further decreases the V_{Ag}^{1-} formation energy through the generation of the complex defect ($V_{Ag}^{1-} + Sn_{Sb}^{1-}$), which has a much lower formation energy than other defects. The preferential formation of the complex defects, controlled by the amount of Sn introduced, not only introduces a higher concentration of holes but also enhances the stability of $AgSbTe_2$. This is supported by experimental measurements of charge carrier density over 5–200 K temperature range, obtained using the four-probe method (Figs. S2 and S3). The partial density of states (DOS), as illustrated in Fig. 2e, f, provides additional validation regarding the efficacy of Sn incorporation in decreasing the contribution of the Te-5p states within the $AgSbTe_2$ system, thereby improving its inherent instability. Overall, Sn doping triggers a synergistic enhancement in hole concentration by modulating the band structure and altering the defect formation energy while at the same time playing a critical role in stabilizing the $AgSbTe_2$ structure.

Due to the random occupation of Ag and Sb ions within the cation sublattice of $AgSbTe_2$, we subsequently investigated the effect of Sn doping on the resulting atomic disorder. Atomic disorder represents a great challenge across several TE materials. The exploration of how atomic disorder affects electronic transport traces back to the 1930s[37–41], with initial observations made in Si-Ge and metal alloys. Within solid solutions, defects resulting from atomic disorder serve as scattering centers of charge carriers, consequently limiting their mean free path. Simultaneously, this disorder induces fluctuations in local potential energy, leading to additional scattering of charge carriers and a reduction in their mobility.

Cation doping has been frequently used to enhance Ag/Sb ordering, resulting in the appearance of cation-ordered nanoscale domains (2–4 nm) within polycrystalline $AgSbTe_2$ matrices[20–23]. These nanodomains play a critical role in reducing lattice thermal conductivity. Moreover, the improved cationic ordering serves to disperse disorder-induced localized electronic states, thereby triggering an enhancement in electrical transport properties. Our results show that Sn doping induces a more chaotic lattice structure. High-resolution high-angle annular dark-field scanning transmission electron microscopy (HAADF-STEM) micrograph confirm the presence of a face-centered cubic phase (space group: Fm-3m) with a lattice parameter of $a = 0.608$ nm for the Sn-doped $AgSbTe_2$ samples (Fig. 3a). Notably, multiple double-diffraction spots observed in the power spectrum of $AgSb_{0.94}Sn_{0.06}Te_2$, circled in red and green, arise from structure disruption within the $AgSbTe_2$ structure. The composite map obtained from inverse fast Fourier transform (FFT) images in Fig. 3b affirms that the double-diffraction spots are not associated with precipitate-like structures but are generated by the disarrayed lattice. The individual FFT images obtained from the green-circled and red-circled diffraction spots unambiguously reveal the presence of a disrupted structure, particularly in the region circled in red.

The disrupted lattice structure arises from multiple short-range Ag/Sb cation-ordering domains within the matrix of Sn-doped $AgSbTe_2$ (Fig. 3c). In the selected area diffraction pattern derived from the HRTEM micrograph of a $AgSb_{0.94}Sn_{0.06}Te_2$ grain (Fig. 3d), weaker diffraction spots observed in Fig. 3e (corresponding to the $AgSbTe_2$ phase, indicated by red arrows) are located halfway between the fundamental spots in the selected area electron diffraction pattern (SADP), indicating a doubling of the unit cell caused by cation ordered

https://doi.org/10.1038/s41467-024-55280-0

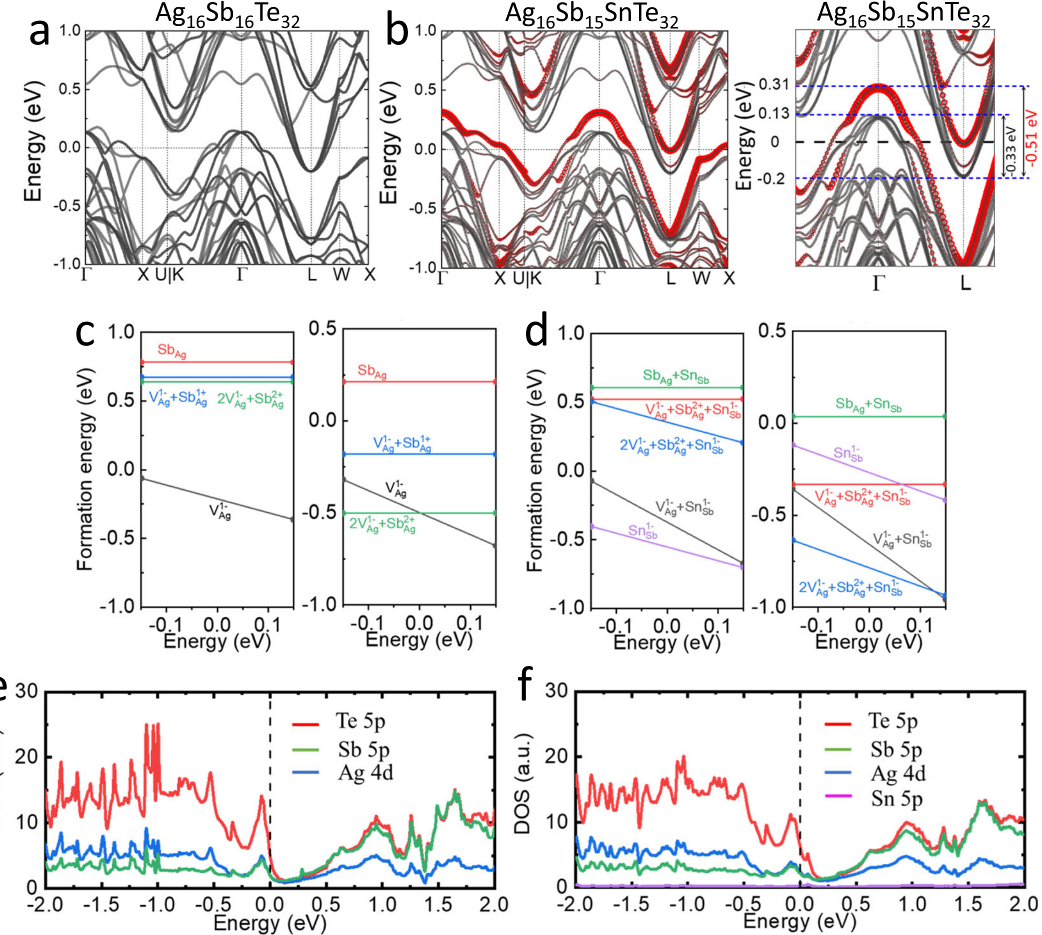

Fig. 2 | Theoretical simulations on band structure, defect formation energy, and density of states. DFT-calculated band structure of (**a**) $Ag_{16}Sb_{16}Te_{32}$ and (**b**) $Ag_{16}Sb_{15}SnTe_{32}$. Defect formation energies of individual defects and complex defects with respect to the Fermi level: (**c**) $Ag_{16}Sb_{16}Te_{32}$ and (**d**) $Ag_{16}Sb_{15}SnTe_{32}$. DOS of (**e**) $Ag_{16}Sb_{16}Te_{32}$ and (**f**) $Ag_{16}Sb_{15}SnTe_{32}$ for the Ag, Sb, and Te atoms. Zero energy corresponds to the Fermi level.

domains in Sn-doped $AgSbTe_2$, consistent with previous works[20,21,23]. Some reflections exhibit double diffractions (marked with red circles in Fig. 3e), suggesting that the short-range cation ordering domains in the sample may not present uniformly. Micrographs in Fig. 3f, g, which show high-resolution TEM (HRTEM) images of the red and green squared regions from Fig. 3d, along with their corresponding FFTs, further display visible double diffractions. These observations, reinforce the conclusion that the structure of Sn-doped $AgSbTe_2$ is more disrupted compared to undoped $AgSbTe_2$ (Fig. S4).

Atomic disorder typically plays a crucial role in inducing additional scattering of charge carriers, thereby reducing their mobility[42–44]. The enhance Ag/Sb atomic ordering by Sn doping should decrease scattering and potentially increase mobility. In pristine $AgSbTe_2$, the carrier concentration is relatively low, around 1.2×10^{18} cm^{-3}, while the hole mobility is high, ~288 cm^2/Vs at room temperature. However, upon Sn doping, the carrier concentration increases to ~3.5×10^{19} cm^{-3}. This substantial increase in carrier concentration is accompanied by a moderate decrease in mobility, with room-temperature carrier mobility dropping to ~31 cm^2/Vs (Table S1). While Sn doping improves cation ordering, the concurrent rise in carrier concentration and the introduction of complex defects generate competing scattering mechanisms that more than offset the potential mobility gains from reduced disorder.

For pristine $AgSbTe_2$, the electrical conductivity (σ) first decreases and then increases with temperature (Fig. 4a). The increase is attributed to the dominance of bipolar contribution, consistent with earlier findings[7,14,18,20]. The bipolar effect starts to be noticed at ~460 K in the undoped $AgSbTe_2$, slightly surpassing that of the Bi_2Te_3 system (350–400 K), consistently with the small band gap of 0.15 eV in Bi_2Te_3[45]. The bipolar phenomenon also degrades the Seebeck coefficients of pristine $AgSbTe_2$ in the high-temperature range measured, as minority carriers (electrons) thermally excited across the band gap counteract the positive Seebeck coefficients associated with free hole diffusion. The Seebeck coefficients of pristine $AgSbTe_2$ increase from 270 μV/K at 300 K to 389 μV/K at 465 K. The high Seebeck coefficient observed in pristine $AgSbTe_2$ arises from the degenerate valence bands and the existence of a mobility edge proximal to the Fermi level, inducing distortions in the electronic density of states and resulting in an enhanced effective mass (m^*). The high Seebeck coefficients measured and the evident bipolar phenomena at high-temperature evidence the semiconductor character of $AgSbTe_2$.

Upon the substitution of Sn^{2+} at the Sb^{3+} site, the electrical conductivity shows a significant enhancement over the whole temperature range, with values escalating from 89 S/cm for pristine $AgSbTe_2$ to 231 S/cm for $AgSb_{0.94}Sn_{0.06}Te_2$ at room temperature. Sn doping in $AgSbTe_2$ introduces holes, resulting in an increase in carrier concentration, as demonstrated in Fig. 4b, based on measurements using the van der Pauw method over the temperature range of 300–670 K. Consistent trends are observed in both low-temperature (Figs. S2 and S3) and high-temperature (Fig. 4b, c) carrier concentration measurements, confirming that Sn incorporation effectively enhances hole concentration. However, the carrier concentrations obtained in the low-temperature range are higher than those measured at high temperatures. This discrepancy is attributed to

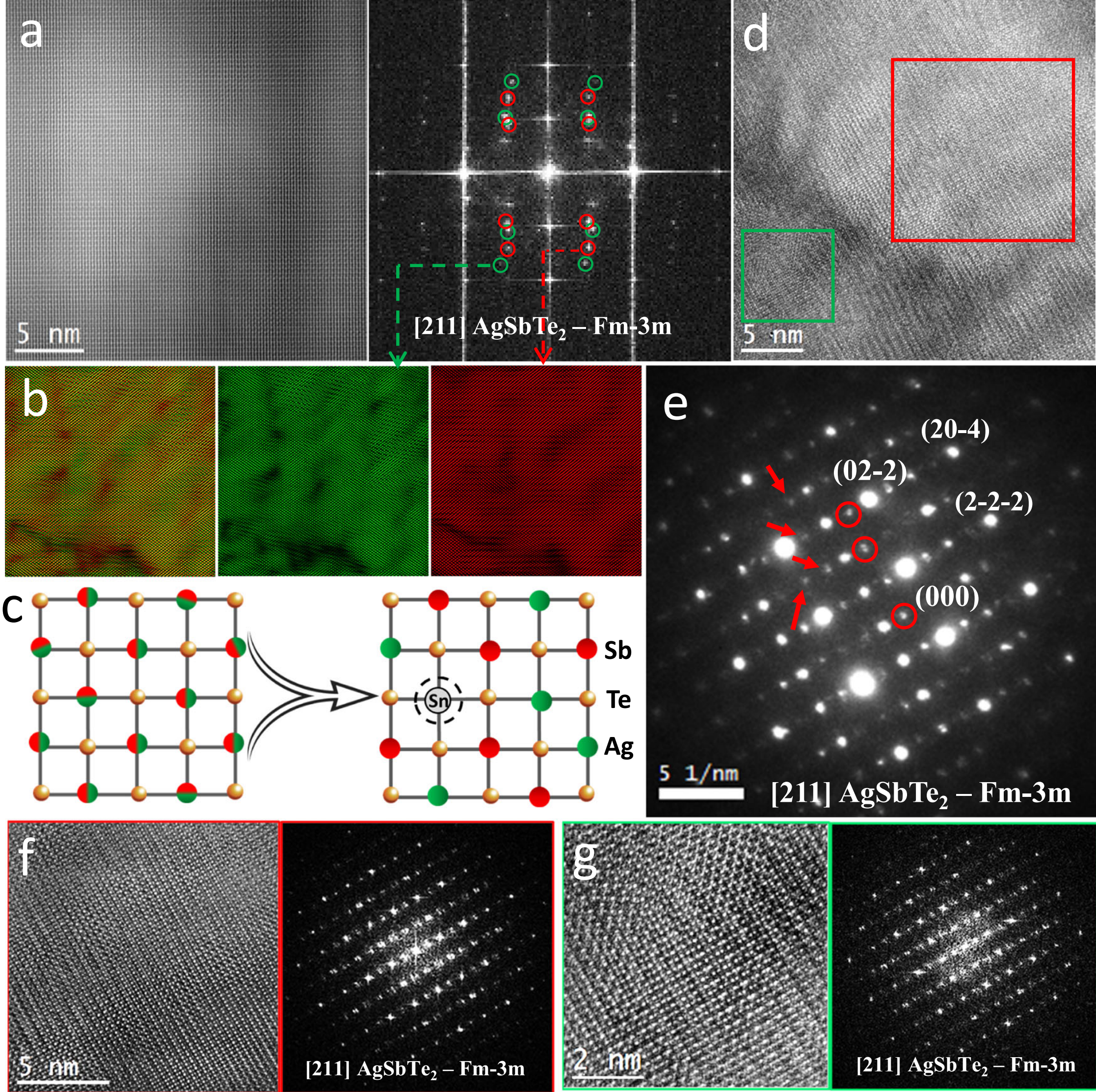

Fig. 3 | Microstructure characterization on $AgSb_{0.94}Sn_{0.06}Te_2$ sample. a Atomic resolution HAADF-STEM image obtained from $AgSb_{0.94}Sn_{0.06}Te_2$ sample and its corresponding FFT, the presence of double-diffraction spots are circled in red and green. **b** Inverse composite and individual FFT images obtained from the red and green circled diffraction spots from panel a. **c** Schematic illustration of Sn doping induced short-range Ag/Sb ordering in $AgSbTe_2$. **d** HRTEM micrograph of a $AgSb_{0.94}Sn_{0.06}Te_2$ grain visualized along its [211] zone axis and (**e**) corresponding selected area diffraction pattern. HRTEM images and corresponding FFTs of the (**f**) red and (**g**) green squared regions in (**d**).

differences in the magnetic field strength and data processing methodologies employed in the respective measurement techniques.

Furthermore, the effect of Sn doping on carrier concentration is non-linear across different doping levels. At a 3% Sn doping level, the substitution efficiently introduces hole carriers and predominantly forms simple Sn-related defects, resulting in a substantial increase in carrier concentration. However, at 6% Sn doping, the emergence of compensating defect complexes, such as $(2V_{Ag}^{1-} + Sb_{Ag}^{2+})$, $(Sb_{Ag}^{2+} + Sn_{Sb}^{1-})$, $(2V_{Ag}^{1-} + Sb_{Ag}^{2+} + Sn_{Sb}^{1-})$, and enhanced impurity interactions lead to increased carrier scattering and a decrease in net carrier concentration. A higher doping level of 10% Sn could introduce significant local structural distortions in the $AgSbTe_2$ matrix, potentially altering the band structure, e.g., shifts in the positions of the conduction band minimum or valence band maximum or even induce changes in the DOS near the Fermi level, that could impact both carrier concentration and mobility. Correspondingly, the carrier mobility presents a reverse trend, indicating that mobility is strongly influenced by carrier-carrier scattering and impurity interactions present in the material. The optimal doping concentration, yielding the highest σ from 300 K to 673 K, was 6 mol% Sn doping, as depicted in Fig. 4a. In addition, elevated temperatures can cause thermal excitation of electrons into the conduction band and carrier trapping by localized states, leading to a reduction in the net carrier concentration in Sn-doped $AgSbTe_2$ with increasing temperature.

The introduction of Sn resulted in a reduction in the Seebeck coefficient due to the increased charge carrier concentration. However, the doped samples still demonstrated decent Seebeck coefficients values, exceeding 170 μV/K across the entire temperature range, as shown in Fig. 4d. Although the upward trend of the Seebeck coefficient in the Sn-doped samples was moderated, a mild increase was still observed beyond 460 K, attributed to a significant reduction in the bipolar effect. While bipolar conduction was not entirely suppressed, it was substantially reduced compared to pristine $AgSbTe_2$. The sustained Seebeck coefficients stem primarily from the significant decrease in electrons and the alteration in band structure upon Sn doping, characterized by band flattening and splitting, thereby inducing an increased m^* conducive to sustaining relatively high Seebeck coefficients.

https://doi.org/10.1038/s41467-024-55280-0

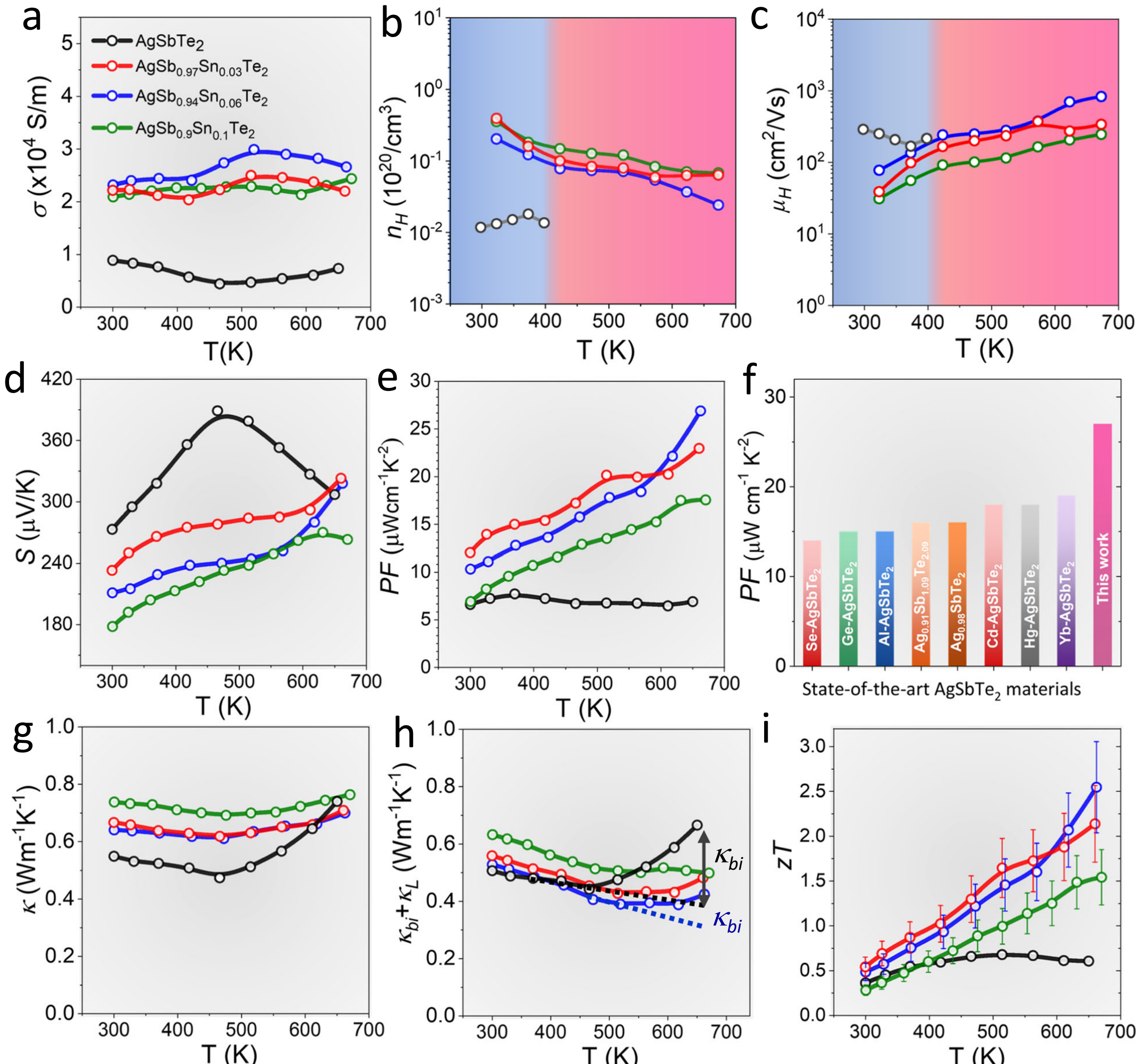

Fig. 4 | Transport properties of $AgSb_{0.94}Sn_{0.06}Te_2$ sample. Temperature-dependent TE properties of $AgSb_{1-x}Sn_xTe_2$. **a** Electric conductivity, *σ*. **b** Carrier concentration, n_H. **c** Mobility, μ_H. **d** Seebeck coefficient, *S*. **e** Power factors, *PF*. **f** Maximum PF comparison with state-of-art $AgSbTe_2$ materials[6,13,14,18,20–23]. **g** Thermal conductivity, *κ*. **h** Combination of bipolar and lattice contribution to the thermal conductivity. **i** TE figure of merit, *zT*, the uncertainty of *zT* measurement is ~20% as indicated by error bar.

This combination of substantial enhancement of electrical conductivities and sustained high Seebeck coefficients in $AgSb_{0.94}Sn_{0.06}Te_2$ resulted in greatly increased *PF* compared to pristine $AgSbTe_2$ throughout the entire temperature range (Fig. 4e). The peak *PF* for $AgSb_{0.94}Sn_{0.06}Te_2$ was observed at 673 K, reaching 27 $\mu Wcm^{-1}K^{-2}$, surpassing the values reported in $Cu_{2-x}Se$[46–48], PbTe[30,49], SnTe[33,50], etc., and to the best of our knowledge, being the highest *PF* reported for $AgSbTe_2$, as illustrated in Fig. 4f. The *PF* attained is comparable to that of commercial Bi_2Te_3-based materials characterized by higher thermal conductivities[51,52], denoting commendable powder density and conversion efficiency in TE generators.

The total thermal conductivity (*κ*) of pristine $AgSbTe_2$ initially decreases with increasing temperature, dropping from 0.55 W/m·K at 300 K to 0.48 W/m·K around 450 K (Fig. 4g), and then increased. This rise in thermal conductivity is attributed to the contribution of bipolar thermal conductivity (κ_{bi}), as illustrated in Figs. 4h and S5. The inherently low thermal conductivity of pure $AgSbTe_2$ aligns with previous studies that identify it as exhibiting glass-like ultralow intrinsic thermal conductivity, attributed to the strong anharmonicity in the defects, stacking faults, and spontaneously formed nanoscale impurity phase[6,7,15,18,20]. In contrast, Sn-doped $AgSbTe_2$ demonstrates higher *κ* values compared to the pristine material. This increase is primarily due to enhanced electronic thermal conductivity (κ_e) and a slight elevation in κ_L. The increase in κ_L can be attributed to the elimination of the nanostructed Ag_2Te impurity phase upon Sn doping, which reduces phonon scattering centers and consequently allows for more efficient heat transport through the lattice. While previous studies on Hg[21], Yb[22], and Cd[20] doping in $AgSbTe_2$ have reported decreases in lattice thermal conductivity, our study observes an increase in κ_L suggesting that the specific nature of the doping element and its interactions within the matrix play a critical role in determining the overall thermal behavior.

Besides, upon partial substitution of Sn for Sb in $AgSbTe_2$, although complete suppression of the bipolar effect was not achieved,

https://doi.org/10.1038/s41467-024-55280-0

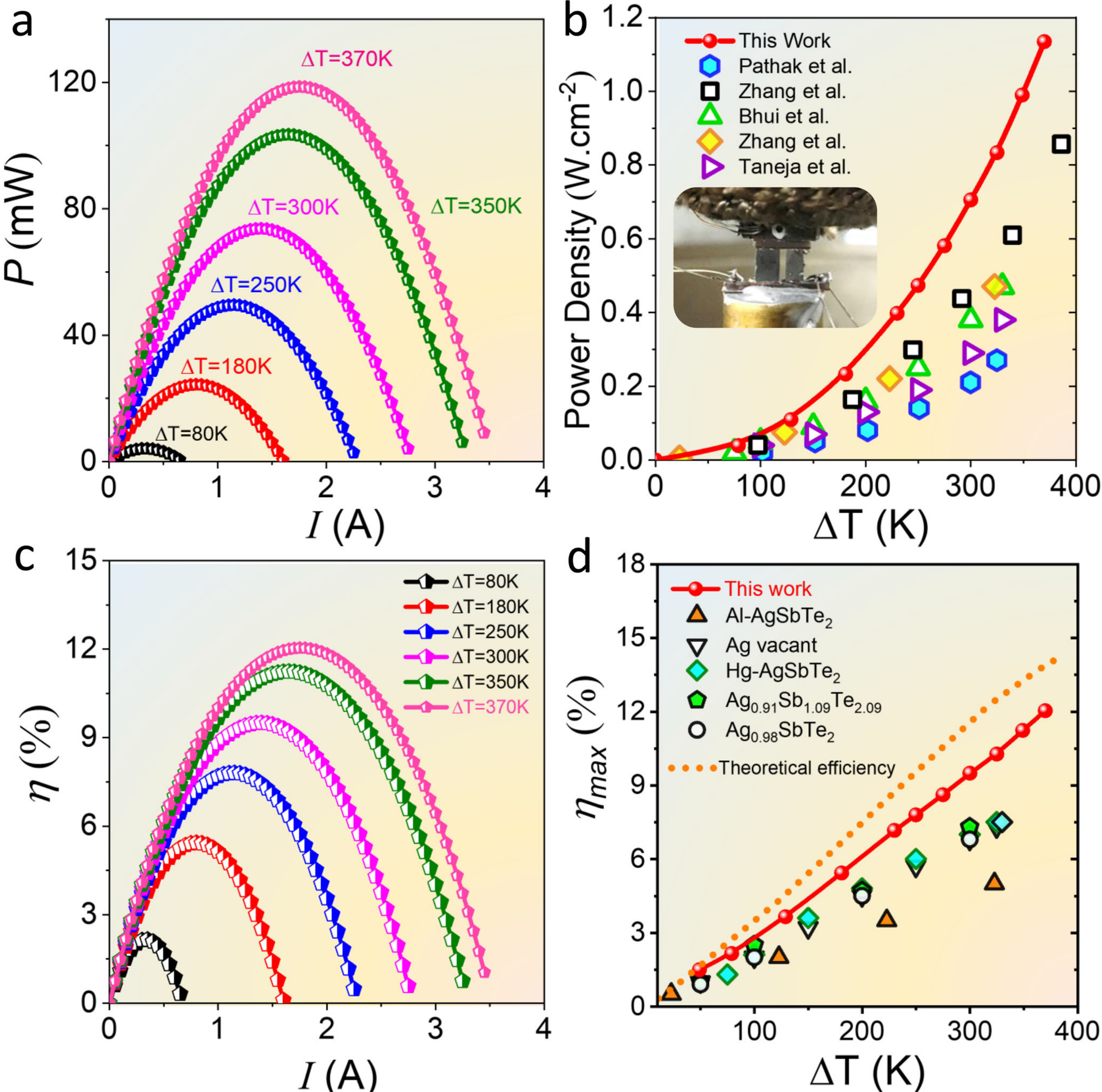

Fig. 5 | Device performance. **a** Current dependent output power of an $AgSb_{0.94}Sn_{0.06}Te_2$ / $Yb_{0.25}Co_{3.75}Fe_{0.25}Sb_{12}$ unicouple module. **b** Maximum power density as a function of *ΔT*. **c** Current-dependent conversion efficiency (η) of the unicouple module. **d** Comparison of the maximum conversion efficiency (η_{max}) as a function of *ΔT* of the $AgSb_{0.94}Sn_{0.06}Te_2$ unicouple device with that of other state-of-art $AgSbTe_2$ devices[2,13,14,19,21,23].

a significant reduction in the bipolar thermal conductivity κ_{bi} was observed. Sn doping in $AgSbTe_2$ reduces the bipolar effect by increasing the ratio of majority carriers (n_h) to minority carriers (n_e). This occurs through the substitution of Sb^{3+} with Sn^{2+}, which introduces additional holes, increases the concentration of V_{Ag}^{1-} that acts as acceptors, and reduces Sb_{Ag}^{2+} antisite defects that would otherwise generate electrons, resulting in a higher n_h/n_e ratio and reduced bipolar conduction. The decrease in κ_{bi}, from 0.25 W/mK in pristine $AgSbTe_2$ to 0.07 W/mK in Sn-doped $AgSbTe_2$ at 660 K (Fig. S5), underscores the role of increased n_h/n_e in reducing the detrimental bipolar contribution. With increasing temperature, the minimum κ_L of the $AgSb_{0.94}Sn_{0.06}Te_2$ sample reaches approximately 0.41 W/mK at around 470 K, higher than κ_L reported in enhanced atomic ordering $AgSbTe_2$ works[20–22]. It is worth noting that one previous work[53] also explored Sn doping in $AgSbTe_2$, but key differences in carrier density, bipolar conduction, and impurity phases were observed compared to our work and recent studies[13,14,17,19,20], which significantly impact transport properties, leading to distinct TE performance.

The enhanced carrier concentration and sustained high Seebeck coefficients in $AgSb_{0.94}Sn_{0.06}Te_2$ yielded exceptional *zT* values, reaching a peak of 2.5 and an average *zT* of 1.32 over the 300–673 K range (Fig. 4i). A *zT* of ~2.5 is among one of the highest values compared with the existing state-of-the-art TE materials (Figs. S6 and S7), highlighting the potential of $AgSbTe_2$ for high-efficiency TE applications in mid-temperature range. Furthermore, the reproducibility of these high *zT* values is confirmed through the analysis of samples from various synthesis batches (Fig. S8) and their performance across multiple heating-cooling cycles (Fig. S9).

Motivated by the noteworthy zT and PF, we proceeded to fabricate a unicouple TE device comprising a p-type $AgSb_{0.94}Sn_{0.06}Te_2$ leg paired with an n-type skutterudite $Yb_{0.25}Co_{3.75}Fe_{0.25}Sb_{12}$ leg[54] (Fig. S11). With a fixed cold-side temperature at 300 K, the open-circuit voltage (V_{oc}) exhibited a linear increase with ΔT (Fig. S12), indicating low contact resistance in the fabricated device, as confirmed by automated scanning four-probe measurements (Fig. S13). The results demonstrate an ultra-low ohmic contact resistance (<1 μΩ·cm^2) between the Cu electrode and the TE legs. Notably, the maximum output power (P_{out}) escalated from 4.5 mW at $\Delta T = 80$ K to 103 mW at $\Delta T = 370$ K as depicted in Fig. 5a, culminating in a calculated power density of 1.13 W/cm^2 (Figs. 5b and S14). Besides, an energy conversion efficiency (η) of 12.1% was derived at a temperature differential of $\Delta T = 370$ K (Fig. 5c, d). The device performance was further validated by simulations of internal resistance, V_{oc}, P_{out}, Q_{in}, and η, based on the dimensions of the p/n legs and their transport properties. The simulation results (Fig. S15) demonstrated slightly higher, yet comparable values for V_{oc}, P_{max}, η_{max}, and power density when compared to experimental data. These minor discrepancies are associated with deviations in input parameters or boundary conditions applied in the simulation, supporting the reliability and consistency of the experimental measurements. In addition, thermal treatment and cyclic performance assessments revealed a significant enhancement in the thermal stability of the Sn-doped materials and devices (Fig. S16). Future studies could focus on evaluating the material's stability over extended periods, which is crucial for the practical application and reliability of TE devices.

To summarize, the charge carrier density of polycrystalline $AgSbTe_2$ was optimized by doping with Sn. The substitution of Sb with Sn facilitated the formation of an impurity band above the VBM. Additionally, the incorporation of Sn suppressed bipolar effects and inhibited the formation of n-type Ag_2Te, leading to relatively higher Seebeck coefficients. Consequently, $AgSb_{0.94}Sn_{0.06}Te_2$ alloys exhibited high power factors of up to 27 μWcm^{-1}K^{-2}. Besides, Sn doping also induced a more chaotic lattice structure characterized by a minimum lattice thermal conductivity of 0.41 W m^{-1} K^{-1}. Although this enhanced disruption did not effectively reduce the lattice thermal conductivity of $AgSbTe_2$, the excellent PF compensated for this limitation. Overall, $AgSb_{0.94}Sn_{0.06}Te_2$ achieved a peak zT of 2.5 at 673 K and a zT_{ave} of 1.32 from 300 to 673 K, outperforming most current state-of-the-art p-type materials in the mid-temperature range. We further engineered a unicouple module with minimized contact resistance, achieving an energy conversion efficiency of up to 12.1% and a power density of up to 1.13 W/cm^2 at ΔT of 370 K. Overall, this work provided cutting-edge insights into engineering high-performance medium-temperature TE materials and devices for efficient waste heat recovery.

Methods

Materials and synthesis

Silver shots (Ag, 99.9% Thermo Scientific), antimony shots (Sb, Alfa Aesar 99.9999%), tin powder (Sn, Sigma Aldrich 99.99%), and tellurium lumps (Te, Alfa Aesar 99.9 %) were used as received, without further purification. $AgSb_{1-x}Sn_xTe_2$ samples were produced by mixing high-purity Ag, Sb, Te, and Sn within quartz tubes. The tubes were sealed under vacuum (~10^{-4} Pa) and slowly heated from room temperature to 1173 K over 6 h, kept at 1173 K for another 6 h, and then slowly cooled down to room temperature for 10 h. The obtained bulk ingots were pulverized to powder and re-consolidated by spark plasma sintering (SPS, Dr. Sinter-625V, Fuji, Japan) at 703 K under a pressure of 40 MPa for 2 min. All consolidated cylinders presented relative densities above 95% of the theoretical value.

Materials characterization

The electrical conductivity and Seebeck coefficient were measured simultaneously (ULVAC-RIKO ZEM-3 system, Japan) using 2 × 2 × 12 mm bars. We estimate an error of ca. 5% in the measurement of both electrical conductivity and the Seebeck coefficient. Temperature-dependent thermal properties were determined by measuring thermal diffusivity with a laser flash system (LFA-467 HT HyperFlash®, Germany). Specific heat was measured on a differential scanning calorimeter (Netzsch DSC 214, Germany, heating/cooling rate of 15 K/min). The thermal conductivity, κ_{total}, was calculated from $\kappa_{total} = D \times \rho \times Cp$, where D, ρ, and Cp are thermal diffusivity, density, and specific heat, respectively. The density is measured using the Archimedes method. The estimated error in thermal conductivity measurement is estimated at about ±4%. Electronic thermal conductivity (κ_e) of $AgSb_{1-x}Sn_xTe_2$ is calculated from Wiedemann-Franz law, $\kappa_e = L\sigma T$, where L and σ, are Lorenz number and electrical conductivity. The Lorenz number is calculated based on the measured Seebeck coefficient: $L = [1.5 + exp\ (-|S|/(116\ \mu VK^{-1}))]\ 10^{-8}\ W\Omega K^{-2}$, proposed by G. J. Snyder et al[55]. The results presented here are an average of the results obtained after measuring 3 pellets produced under identical conditions. Measurements between different samples have standard deviations below 10%.

X-ray diffraction analysis was carried out on a PANalytical Empyrean with Cu-K$_\alpha$ radiation in 2θ angle range of 10–60°. High temperature (>300 K) charger carrier density and mobility were characterized by a LakeShore Hall Effect System (8400 Series HMS, LakeShore), using four-contact van der Pauw sample configurations with magnetic field of 0.9 T. Low temperature hall resistivity, ρ_{xy} were performed using a standard four-probe technique in a physical properties measurement system (PPMS, Quantum Design) from 2.2 to 250 K up to 9 T. The field dependences of ρ_{xy} is obtained using $\rho_{xy} = [\rho_{xy}(+\mu_o H) - \rho_{xy}(-\mu_o H)]/2$. Both samples of pristine and doped-$AgSbTe_2$ exhibit non-linear field dependence. Since $\rho_{xy}(H>6T)$ exhibiting linear field dependence, single band model is used and the carrier density n is estimated via $n = (\frac{1}{eR_H})$, where e is the electric charge and R_H is the Hall coefficient that extracted from the slope of the $\rho_{xy}(H)$. High-resolution transmission electron microscopy (HRTEM) was performed using an FEI Titan G2. TEM samples were prepared by a focused-ion beam (FIB). A field emission scanning electron microscopy (FESEM, FEI Verios G4) operated at 5.0 kV was used to determine the microstructure morphology. Energy-dispersive X-ray spectroscopy (EDX) on an Oxford Aztec spectrometer attached to FEI Verios G4 SEM at 20.0 kV was used to measure the material composition. X-ray photoelectron spectroscopy (XPS) experiments were performed using a Physical Electronics VersaProbe III instrument equipped with a monochromatic Al kα X-ray source ($h\nu = 1{,}486.6$ eV) and a concentric hemispherical analyzer. Charge neutralization was performed using both low-energy electrons (<5 eV) and argon ions. Peaks were charge referenced to CH_x band in the carbon 1 s spectra at 284.8 eV. Measurements were made at a take-off angle of 50° with respect to the sample surface plane. Quantification was done using instrumental relative sensitivity factors that account for the X-ray cross-section and inelastic mean free path of the electrons. The analyzed area was ~200 μm in diameter.

Density functional theory (DFT) calculations

The projector augmented wave (PAW) method[56] as implemented in Vienna Ab-initio Simulation Package (VASP)[57] was adopted to perform the first-principles calculations. The exchange-correlation energy was calculated by using the revised generalized gradient approximation (GGA) Perdew-Burke-Ernzerhof (PBEsol)[58,59]. The plane-wave cutoff energy was set to 500 eV for all calculations. A Monkhorst-Pack Γ-centered 11 × 11 × 11 $\boldsymbol{k}$ mesh is used for Brillouin zone sampling. The well-studied $Fd\bar{3}m$ $AgSbTe_2$ conventional cell (64 atoms) was selected as the initial structure. The internal position of atoms was fully relaxed until the residual force between atoms was smaller than 0.01 eV Å^{-1} and the total energy reached the convergency 10^{-8} eV. The electronic band

structure and density of states were calculated based on the fully relaxed structure.

Defect calculations

The formation energy $E(\alpha,q,f)$ of a defect α with q charge is defined as:

$$E(\alpha, q, f) = E_{\text{defect}} - E_{\text{perfect}} + \sum_i \eta_i \mu_i + q(f + E_{\text{VBM}} + \Delta) \tag{1}$$

where E_{defect} and E_{perfect} are the total energy of $AgSbTe_2$ and $AgSb_{1-x}Sn_xTe_2$ with and without charged defects, respectively. n_i refers to the number of α atoms added to or removed from the perfect cell. μ_i is the chemical potential of atom α, which can be obtained by the formation of $AgSbTe_2$:

$$\mu_{Ag} + \mu_{Sb} + 2\mu_{Te} = E_f(AgSbTe_2) \tag{2}$$

where $E_f(AgSbTe_2)$ is the formation of $AgSbTe_2$. The second impurity Ag_2Te and SnTe should be avoided:

$$2\mu_{Ag} + \mu_{Te} < E_f(Ag_2Te) \tag{3}$$

$$\mu_{Sn} + \mu_{Te} < E_f(S_nT_e) \tag{4}$$

The equation and inequality above defined a three-dimensional phase space of μ_{Ag}, μ_{Sb} and μ_{Te}.

To simplify the question, we assume there is always excess Tellurium during the synthesis process, which means $\mu_{\text{Te}} = 0$.

COMSOL multiphysics simulation analysis

The TE module performance was simulated using COMSOL Multiphysics 6.2[60,61], employing a p-type $AgSb_{0.94}Sn_{0.06}Te_2$ leg paired with an n-type skutterudite $Yb_{0.25}Co_{3.75}Fe_{0.25}Sb_{12}$ leg. The simulation accounted for TE effects, electromagnetic-thermal interactions, and temperature-dependent material properties. Material parameters for components such as copper and alumina were sourced from the default database. Appropriate boundary conditions and assumptions were applied, treating the TE module as a steady-state, adiabatic system, with heat radiation and convection on all surfaces neglected. The cold-side temperature was fixed at 300 K, while the hot-side temperature was varied to maintain a consistent temperature gradient. Electrical and thermal contact resistances were set to 5×10^{-6} Ω·cm^2 and 5×10^{-6} KW·m^{-2}, respectively, in this theoretical design.

Module fabrication and testing

The unicouple module was fabricated based on the techniques reported in our previous work[19,62]. The p-type $AgSb_{0.94}Sn_{0.06}Te_2$ leg, with Ni as diffusion-barrier layers and Cu as electrodes, was fabricated by firstly spark plasma sintering the powders of $AgSb_{0.94}Sn_{0.06}Te_2$ at 703 K under a pressure of 40 MPa for 2 min. The obtained bulk pellet was polished and cleaned thoroughly by ultrasonic stirring. The pellet was then diced along the press direction into a certain dimension (P-leg: 2.7 mm (length) × 2.9 mm (width) × 4.8 mm (height)) legs using a wire saw. The reported $Yb_{0.25}Co_{3.75}Fe_{0.25}Sb_{12}$ skutterudite material by Li et al[54]. was used as the n-type leg. The pellet was then diced along the press direction into a certain dimension leg (N-leg: 1.9 mm (length) × 1.4 mm (width) × 4.8 mm (height)) using a wire saw. The obtained bulk pellet was polished and cleaned in ethanol thoroughly by ultrasonic stirring. Afterward, a layer of Ni was deposited on the top and bottom side of each leg by electroless nickel plating (~20 μm). The legs were connected by direct bond copper substrates using Gallium-Indium eutectic metal to provide electrical and thermal contact at the junction of thermoelectric leg/header. The output properties of the fabricated unicouple device were measured using a custom-built power generation setup. The measurement method and the testing principle have been explained in our previous works[19,62–65]. The schematic diagram of measurement is described in Fig. S9. The output power and conversion efficiency of the unicouple TEGs were simultaneously measured under vacuum condition (~10^{-9} Torr) from room temperature to 400°C. The hot side temperature was precisely controlled by a heater that provides constant heat flow (Q_{in}) to the top side of the module. TEG converts a portion of this heat into output power (P_{out}) and rejects the rest (Q_{out}) into the Q-meter which is connected to a water-cooled heat sink (cold side) with constant temperature of ~20 °C. The open circuit voltage (V_{oc}) and device voltage (V_d) were recorded at a certain current using a voltmeter (KEITHLEY) and a power supply (KEITHLEY 2200-20-5). Using this information, internal resistance (R_i) and P_{out} were then calculated. The temperatures of hot and cold side were monitored using K-type thermocouples. The system was calibrated thoroughly to minimize the heat loss. The maximum power output from TE modules P_{max} is calculated using the expression:

$$P_{\max} = \frac{V_{oc}^2}{4R_i}$$

where V_{oc} is the measured open-circuit voltage and R_i is the module internal resistance. V_{oc} and device voltage (V_d) were recorded at a certain current using a voltmeter (KEITHLEY) and a power supply (KEITHLEY 2200-20-5). The heat flow (Q_{out}) of unicouple decive is calculated by:

$$Q_{out} = Q_{leg(p)} + Q_{leg(n)} = \kappa_p \times \frac{A_p}{l_p} \times \Delta T + \kappa_n \times \frac{A_n}{l_n} \times \Delta T$$

where κ, A, and ΔT are the thermal conductivity, cross-section area, and temperature difference of TE legs, respectively. Thermal radiation (Q_{rad}) is defined as $Q_{rad} = Q'_{out} - Q_{out}$, where Q'_{out} is measured and calculated from a copper Q-meter which is connected to a water-cooled heatsink. Thermal radiation is determined negligible when ΔT < 420 K in our previous study[19,62], therefore, in this study, Q_{out} is used to represent the heat flow through the TE module. The conversion efficiency of double-leg modules is quantified by:

$$\eta = \frac{P_{out}}{Q_{in}} = \frac{P_{out}}{Q_{out} + P_{out}}$$

where Q_{in} represents the heat flow from heat source. The TE module is measured three times and the average values are reported. The maximum standard deviation of conversion efficiency based on three measurement results is used as uncertainties of conversion efficiency and output power. The uncertainty of output power and conversion efficiency is ±1% and ±3%, respectively.

Reporting summary

Further information on research design is available in the Nature Portfolio Reporting Summary linked to this article.

Data availability

The authors declare that all data supporting the findings of this study are available within the article and its Supplementary Information files or from the corresponding author upon reasonable request.

References

1. Bell, L. E. Cooling, heating, generating power, and recovering waste heat with thermoelectric systems. *Science* **321**, 1457–1461 (2008).
2. Goldsmid, H. J. *Introduction to thermoelectricity*. Vol. 121 (Springer, 2010).
3. Shi, X.-L., Zou, J. & Chen, Z.-G. Advanced thermoelectric design: from materials and structures to devices. *Chem. Rev.* **120**, 7399–7515 (2020).

4. Tan, G., Zhao, L.-D. & Kanatzidis, M. G. Rationally designing high-performance bulk thermoelectric materials. *Chem. Rev.* **116**, 12123–12149 (2016).
5. Snyder, G. J. & Toberer, E. S. Complex thermoelectric materials. *Nat. Mater.* **7**, 105–114 (2008).
6. Hong, M. et al. Achieving zT>2 in p-type $AgSbTe_{2-x}Se_x$ alloys via exploring the extra light valence band and introducing dense stacking faults. *Adv. Energy Mater.* **8**, 1702333 (2018).
7. Lee, J. K. et al. Enhanced thermoelectric properties of $AgSbTe_2$ obtained by controlling heterophases with Ce doping. *Sci. Rep.* **7**, 4496 (2017).
8. Du, B., Li, H., Xu, J., Tang, X. & Uher, C. Enhanced figure-of-merit in Se-doped p-type $AgSbTe_2$ thermoelectric compound. *Chem. Mater.* **22**, 5521–5527 (2010).
9. Ganesan, P. et al. Carrier optimization and reduced thermal conductivity leading to enhanced thermoelectric performance in (Mg, S) co-doped $AgSbTe_2$. *Mater. Today Phys.* **42**, 101358 (2024).
10. Pan, Y., Wang, S., Lai, X. & Jian, J. Enhanced thermoelectric performance of S-Doped $AgSbTe_2$ by synergistic optimization of electrical and thermal transport. *J. Phys. Chem. C* **128**, 1932–7447 (2024).
11. Ye, L.-H. et al. First-principles study of the electronic, optical, and lattice vibrational properties of $AgSbTe_2$. *Phys. Rev. B* **77**, 245203 (2008).
12. Prado-Gonjal, J. et al. Optimizing thermoelectric properties through compositional engineering in ag-deficient $AgSbTe_2$ synthesized by arc melting. *ACS Appl. Electron. Mater.* **6**, 2969–2977 (2024).
13. Gong, Z., Saglik, K., Wu, J., Suwardi, A. & Cao, J. Suppressing Ag 2 Te nanoprecipitates for enhancing thermoelectric efficiency of $AgSbTe_2$. *Nanoscale* **15**, 18283–18290 (2023).
14. Zhang, K. et al. Dual alloying enables high thermoelectric performance in $AgSbTe_2$ by manipulating carrier transport behavior. *Adv. Funct. Mater.* **34**, 2400679 (2024).
15. Cao, J. et al. Non-equilibrium strategy for enhancing thermoelectric properties and improving stability of $AgSbTe_2$. *Nano Energy* **107**, 108118 (2023).
16. Roychowdhury, S., Panigrahi, R., Perumal, S. & Biswas, K. Ultrahigh thermoelectric figure of merit and enhanced mechanical stability of p-type $AgSb_{1-x}Zn_xTe_2$. *ACS Energy Lett.* **2**, 349–356 (2017).
17. Kim, J. H. et al. Enhancement of phase stability and thermoelectric performance of meta-stable AgSbTe2 by thermal cycling process. *Adv. Funct. Mater.* **34**, 2404886 (2024).
18. Chen, B. C., Wang, K. K. & Wu, H. J. Cation modulation in $AgSbTe_2$ realizes carrier optimization, defect engineering, and a 7% single-leg thermoelectric efficiency. *Small* **20**, 2401723 (2024).
19. Zhang, Y. et al. Defect-engineering-stabilized $AgSbTe_2$ with high thermoelectric performance. *Adv. Mater.* **35**, 2208994 (2023).
20. Roychowdhury, S. et al. Enhanced atomic ordering leads to high thermoelectric performance in $AgSbTe_2$. *Science* **371**, 722–727 (2021).
21. Bhui, A. et al. Hg doping induced reduction in structural disorder enhances the thermoelectric performance in $AgSbTe_2$. *J. Am. Chem. Soc.* **145**, 25392–25400 (2023).
22. Taneja, V. et al. High thermoelectric performance in phonon-glass electron-crystal like $AgSbTe_2$. *Adv. Mater.* **36**, e2307058 (2024).
23. Pathak, R. et al. Vacancy controlled nanoscale cation ordering leads to high thermoelectric performance. *Energy Environ. Sci.* **16**, 3110–3118 (2023).
24. Ayral-Marin, R., Brun, G., Maurin, M. & Tedenac, J. Contribution to the study of $AgSbTe_2$. *Eur. J. solid state Inorg. Chem.* **27**, 747–757 (1990).
25. Wyzga, P. & Wojciechowski, K. Analysis of the influence of thermal treatment on the stability of $Ag_{1-x}Sb_{1+x}Te_{2+x}$ and Se-doped $AgSbTe_2$. *J. Electron. Mater.* **45**, 1548–1554 (2016).
26. Shinya, H., Masago, A., Fukushima, T. & Katayama-Yoshida, H. Inherent instability by antibonding coupling in $AgSbTe_2$. *Jpn. J. Appl. Phys.* **55**, 041801 (2016).
27. Liu, Y. et al. Surface chemistry and band engineering in $AgSbSe_2$: toward high thermoelectric performance. *ACS nano* **17**, 11923–11934 (2023).
28. Gong, Y. et al. Divacancy and resonance level enables high thermoelectric performance in n-type SnSe polycrystals. *Nat. Commun.* **15**, 4231 (2024).
29. Hoang, K., Mahanti, S., Salvador, J. R. & Kanatzidis, M. G. Atomic ordering and gap formation in Ag-Sb-based ternary chalcogenides. *Phys. Rev. Lett.* **99**, 156403 (2007).
30. Xiao, Y. et al. Realizing high-performance n-type PbTe by synergistically optimizing effective mass and carrier mobility and suppressing bipolar thermal conductivity. *Energy Environ. Sci.* **11**, 2486–2495 (2018).
31. Xiao, Y. & Zhao, L. Charge and phonon transport in PbTe-based thermoelectric materials. *npj Quantum Mater.* **3**, 55 (2018).
32. Hao, S., Dravid, V. P., Kanatzidis, M. G. & Wolverton, C. Computational strategies for design and discovery of nanostructured thermoelectrics. *npj Comput. Mater.* **5**, 58 (2019).
33. Ibáñez, M. et al. Ligand-mediated band engineering in bottom-up assembled SnTe nanocomposites for thermoelectric energy conversion. *J. Am. Chem. Soc.* **141**, 8025–8029 (2019).
34. Tang, X. et al. Dopant induced impurity bands and carrier concentration control for thermoelectric enhancement in p-type $Cr_2Ge_2Te_6$. *Chem. Mater.* **29**, 7401–7407 (2017).
35. Xie, H. et al. Ultralow thermal conductivity in diamondoid structures and high thermoelectric performance in $(Cu_{1-x}Ag_x)(In_{1-y}Ga_y)Te_2$. *J. Am. Chem. Soc.* **143**, 5978–5989 (2021).
36. Xie, H. et al. High thermoelectric performance in chalcopyrite $Cu_{1-x}Ag_xGaTe_2$-ZnTe: nontrivial band structure and dynamic doping effect. *J. Am. Chem. Soc.* **144**, 9113–9125 (2022).
37. Bragg, W. L. & Williams, E. J. The effect of thermal agitation on atomic arrangement in alloys. *Proc. R. Soc. Lond. Ser. A Contain. Pap. A Math. Phys. Character* **145**, 699–730 (1934).
38. Nix, F. C. & Shockley, W. Order-disorder transformations in alloys. *Rev. Mod. Phys.* **10**, 1 (1938).
39. Williams, E. J. The effect of thermal agitation on atomic arrangement in alloys-III. *Proc. R. Soc. Lond. Ser. A Math. Phys. Sci.* **152**, 231–252 (1935).
40. Nordheim, L. Zur elektronentheorie der metalle. i. *Ann. Der Phys.* **401**, 607–640 (1931).
41. Paul, W. Band structure of the intermetallic semiconductors from pressure experiments. *J. Appl. Phys.* **32**, 2082–2094 (1961).
42. Xie, H. et al. The intrinsic disorder related alloy scattering in ZrNiSn half-Heusler thermoelectric materials. *Sci. Rep.* **4**, 6888 (2014).
43. Xie, H.-H. et al. Interrelation between atomic switching disorder and thermoelectric properties of ZrNiSn half-Heusler compounds. *CrystEngComm* **14**, 4467–4471 (2012).
44. Mi, J.-L. et al. Elaborating the crystal structures of MgAgSb thermoelectric compound: polymorphs and atomic disorders. *Chem. Mater.* **29**, 6378–6388 (2017).
45. Nassary, M., Shaban, H. & El-Sadek, M. Semiconductor parameters of Bi_2Te_3 single crystal. *Mater. Chem. Phys.* **113**, 385–388 (2009).
46. Hu, H. et al. Highly stabilized and efficient thermoelectric copper selenide. *Nat. Mater.* **23**, 527–534 (2024).
47. Yu, B. et al. Thermoelectric properties of copper selenide with ordered selenium layer and disordered copper layer. *Nano Energy* **1**, 472–478 (2012).
48. Xing, C. et al. Thermoelectric performance of surface-engineered $Cu_{1.5-x}Te$-Cu_2Se nanocomposites. *ACS Nano* **17**, 8442–8452 (2023).

49. Ahn, K. et al. Enhanced thermoelectric properties of p-type nanostructured PbTe-MTe (M = Cd, Hg) materials. *Energy Environ. Sci.* **6**, 1529–1537 (2013).
50. Tan, G. et al. Codoping in SnTe: enhancement of thermoelectric performance through synergy of resonance levels and band convergence. *J. Am. Chem. Soc.* **137**, 5100–5112 (2015).
51. Poudel, B. et al. High-thermoelectric performance of nanostructured bismuth antimony telluride bulk alloys. *Science* **320**, 634–638 (2008).
52. Liu, Y. et al. High thermoelectric performance in crystallographically textured n-type $Bi_2Te_{3-x}Se_x$ produced from asymmetric colloidal nanocrystals. *ACS Nano* **12**, 7174–7184 (2018).
53. Mohanraman, R. et al. Influence of nanoscale Ag_2Te precipitates on the thermoelectric properties of the Sn doped P-type $AgSbTe_2$ compound. *APL. Mater.* **2**, 096114 (2014).
54. Li, W. et al. Enhanced thermoelectric performance of Yb-single-filled skutterudite by ultralow thermal conductivity. *Chem. Mater.* **31**, 862–872 (2019).
55. Kim, H.-S., Gibbs, Z. M., Tang, Y., Wang, H. & Snyder, G. J. Characterization of Lorenz number with Seebeck coefficient measurement. *APL Mater.* **3**, 041506 (2015).
56. Blöchl, P. E. Projector augmented-wave method. *Phys. Rev. B* **50**, 17953 (1994).
57. Kresse, G. & Furthmüller, J. Efficient iterative schemes for ab initio total-energy calculations using a plane-wave basis set. *Phys. Rev. B* **54**, 11169 (1996).
58. Perdew, J. P. et al. Restoring the density-gradient expansion for exchange in solids and surfaces. *Phys. Rev. Lett.* **100**, 136406 (2008).
59. Perdew, J. P., Burke, K. & Ernzerhof, M. Generalized gradient approximation made simple. *Phys. Rev. Lett.* **77**, 3865 (1996).
60. Xu, G., Duan, Y., Chen, X., Ming, T. & Huang, X. Effects of thermal and electrical contact resistances on the performance of a multi-couple thermoelectric cooler with non-ideal heat dissipation. *Appl. Therm. Eng.* **169**, 114933 (2020).
61. Ouyang, Z. & Li, D. Modelling of segmented high-performance thermoelectric generators with effects of thermal radiation, electrical and thermal contact resistances. *Sci. Rep.* **6**, 1 (2016).
62. Li, W. et al. Bismuth telluride/half-Heusler segmented thermoelectric unicouple modules provide 12% conversion efficiency. *Adv. Energy Mater.* **10**, 2001924 (2020).
63. Ghosh, S. et al. High-entropy-driven half-Heusler alloys boost thermoelectric performance. *Joule* (2024).
64. Zhu, H. et al. Half-Heusler alloys as emerging high power density thermoelectric cooling materials. *Nat. Commun.* **14**, 3300 (2023).
65. Li, W. et al. Toward high conversion efficiency of thermoelectric modules through synergistical optimization of layered materials. *Adv. Mater.* **35**, 2210407 (2023).

Acknowledgements

This work is primarily supported by US ARMY Devcom through SBIR program. B.P. acknowledges the financial support from the Army RIF program (No. W911W6-19-C-0083). Y.Z. & C.X. acknowledge the financial support from Wenzhou Science and Technology Bureau (No. G20240034 and No. G20240041) and Institute of Wenzhou-Zhejiang Unviersity (XMGL-CX–202303). D.W. acknowledges the financial support from the National Natural Science Foundation of China (No. 12204156) and the China Postdoctoral Science Foundation (Nos. 2023TQ0315 and 2023M743224). K.H.L. acknowledges the financial support of the National Natural Science Foundation of China (Grant No. 22208293). Y.L acknowledges funding from the National Natural Science Foundation of China (Grants No. 22209034). S.H.L. & Z.Q.M. acknowledge the support by NSF through the Penn State 2D Crystal Consortium - Materials Innovation Platform (2DCC-MIP) under NSF Cooperative Agreement No. DMR-2039351.

Author contributions
Y.Z. designed this work. Y.Z. and C.X. synthesized the samples and carried out the transport property measurements. L.Z. analyzed the XPS results. A.G. contributed to the TEM analysis. Y.L., L.K.H., H.Z., S.H.L., C.C., and S.C. discussed the content of the paper. Z.L., M.H., R.B.S., and D.W. contributed to the DFT and COMSOL calculations. Y.Z. wrote the manuscript. X.F., T.Z., Z.M., L.D.Z, A.C., and B.P. edited the manuscript.

Competing interests
One Chinese patent application (202410992695X) was filed by Y.Z. and T.Z. The remaining authors declare no competing interests.

Additional information
Supplementary information The online version contains supplementary material available at https://doi.org/10.1038/s41467-024-55280-0.

Correspondence and requests for materials should be addressed to Yu Zhang, Tiejun Zhu or Bed Poudel.

Peer review information *Nature Communications* thanks the anonymous reviewer(s) for their contribution to the peer review of this work. A peer review file is available.

Reprints and permissions information is available at http://www.nature.com/reprints

Publisher's note Springer Nature remains neutral with regard to jurisdictional claims in published maps and institutional affiliations.

Open Access This article is licensed under a Creative Commons Attribution-NonCommercial-NoDerivatives 4.0 International License, which permits any non-commercial use, sharing, distribution and reproduction in any medium or format, as long as you give appropriate credit to the original author(s) and the source, provide a link to the Creative Commons licence, and indicate if you modified the licensed material. You do not have permission under this licence to share adapted material derived from this article or parts of it. The images or other third party material in this article are included in the article's Creative Commons licence, unless indicated otherwise in a credit line to the material. If material is not included in the article's Creative Commons licence and your intended use is not permitted by statutory regulation or exceeds the permitted use, you will need to obtain permission directly from the copyright holder. To view a copy of this licence, visit http://creativecommons.org/licenses/by-nc-nd/4.0/.

© The Author(s) 2024

[1]Institute of Wenzhou, Zhejiang University, Wenzhou, China. [2]Department of Materials Science and Engineering, Pennsylvania State University, University Park, PA, USA. [3]Henan Key Laboratory of Diamond Optoelectronic Materials and Devices, Key Laboratory of Material Physics, Ministry of Education, School of Physics, Zhengzhou University, Zhengzhou, China. [4]Cardiff Catalysis Institute, School of Chemistry, Cardiff University, Cardiff, UK. [5]2D Crystal Consortium, Materials Research Institute, The Pennsylvania State University, University Park, PA, USA. [6]Department of Physics, The Pennsylvania State University, University Park, PA, USA. [7]School of Materials Science and Engineering, Beihang University, Beijing, China. [8]Department of Materials Science and Engineering, Northwestern University, Evanston, IL, USA. [9]Institute of Zhejiang University-Quzhou, Quzhou, China. [10]Beijing National Laboratory for Condensed Matter

Physics, Institute of Physics, Chinese Academy of Sciences, Beijing, China. [11]Department of Mechanical Engineering, Pennsylvania State University, University Park, PA, USA. [12]Anhui Province Key Laboratory of Advanced Catalytic Materials and Reaction Engineering, School of Chemistry and Chemical Engineering, Hefei University of Technology, Hefei, China. [13]Centre for Future Materials, and School of Engineering, University of Southern Queensland, Springfield Central, Queensland, Australia. [14]Department of Chemical Engineering, School of Engineering, The University of Manchester Oxford Road, Manchester, UK. [15]Catalonia Institute for Energy Research-IREC, Sant Adrià de Besòs, Barcelona, Catalonia, Spain. [16]ICREA, Pg. Lluis Companys, Barcelona, Catalonia, Spain. [17]State Key Laboratory of Silicon and Advanced Semiconductor Materials, and School of Materials Science and Engineering, Zhejiang University, Hangzhou, China. [18]These authors contributed equally: Yu Zhang, Congcong Xing. ✉e-mail: yzhangpeter@163.com; zhutj@zju.edu.cn; bup346@psu.edu